First-principles real-space study of electronic and optical excitations in rutile TiO_2 nanocrystals

Linda Hung,* Kopinjol Baishya, and Serdar Öğüt†
Department of Physics, University of Illinois at Chicago, Chicago, Illinois 60607, USA
(Received 28 August 2014; published 17 October 2014)

We model rutile titanium dioxide nanocrystals (NCs) up to ∼1.5 nm in size to study the effects of quantum confinement on their electronic and optical properties. Ionization potentials (IPs) and electron affinities (EAs) are obtained via the perturbative GW approximation (G_0W_0) and ΔSCF method for NCs up to 24 and 64 TiO_2 formula units, respectively. These demanding GW computations are made feasible by using a real-space framework that exploits quantum confinement to reduce the number of empty states needed in GW summations. Time-dependent density functional theory (TDDFT) is used to predict the optical properties of NCs up to 64 TiO_2 units. For a NC containing only 2 TiO_2 units, the offsets of the IP and the EA from the corresponding bulk limits are of similar magnitude. However, as NC size increases, the EA is found to converge more slowly to the bulk limit than the IP. The EA values computed at the G_0W_0 and ΔSCF levels of theory are found to agree fairly well with each other, while the IPs computed with ΔSCF are consistently smaller than those computed with G_0W_0 by a roughly constant amount. TDDFT optical gaps exhibit weaker size dependence than GW quasiparticle gaps, and result in exciton binding energies on the order of eV. Altering the dimensions of a fixed-size NC can change electronic and optical excitations up to several tenths of an eV. The largest NCs modeled are still quantum confined and do not yet have quasiparticle levels or optical gaps at bulk values. Nevertheless, we find that classical Mie-Gans theory can quite accurately reproduce the line shape of TDDFT absorption spectra, even for (anisotropic) TiO_2 NCs of subnanometer size.

DOI: 10.1103/PhysRevB.90.165424 PACS number(s): 73.22.−f, 78.67.Bf, 71.15.Qe

I. INTRODUCTION

Titanium dioxide (TiO_2) is among the most studied transition-metal oxides. Scientific and technological interest in TiO_2 is primarily driven by its various uses related to solar energy; its photocatalytic, photoelectric, and photochemical properties make up several active areas of research [1]. However, bulk polymorphs of TiO_2 absorb light in the UV range, so they can only use a fraction of the energy from the solar spectrum. Accordingly, much ongoing research has focused on understanding and tuning the electronic and optical properties of TiO_2, with the ultimate goal of increasing the efficiency of a variety of applications. One method of altering energy levels and absorption wavelengths is dye sensitization [2,3]. Dye-sensitized solar cells (DSSCs) have many practical advantages, including prospective low-cost fabrication and enhanced performance over a range of conditions. Another area of research involves the morphology of TiO_2, with nanowires, nanoclusters, and other nanostructures being synthesized and their properties explored [4–6]. Among these new forms of TiO_2, quantum confinement effects have been observed experimentally only at the smallest scales (clusters with diameters smaller than 2 nm) [7–11].

To better understand the electronic and optical properties of TiO_2, a variety of first-principles methods have also been used [12]. Density functional theory (DFT) generally can describe ground-state properties, but more computationally expensive theories are necessary when modeling electronically and optically excited states [13]. Time-dependent DFT (TDDFT) and Green's function methods such as the GW approximation and the Bethe-Salpeter equation (BSE) offer a good balance of accuracy and efficiency for these applications [14], and for bulk rutile, anatase, and brookite TiO_2, GW and BSE have been found to give quasiparticle band gaps and optical spectra in good agreement with experiment [15–17]. However, crystalline bulk TiO_2 can be represented by only 2 (for rutile and anatase) or 8 (for brookite) TiO_2 formula units, while nanostructures can contain tens of TiO_2 units or more. Therefore, due to the significant cost of many-body perturbation theory, past simulations of nanowires [18–22] or clusters [23–27] at the nanoscale have been mostly performed at the DFT level. Similarly, a majority of optical studies of nanostructured TiO_2 have been performed with time-dependent tight-binding [28] and TDDFT using semilocal exchange-correlation or hybrid functionals [29–32].

Even for systems small enough to be treated with many-body perturbation theory, it can be challenging to construct simulations with physical relevance. Attempts to validate computational methods with experimental measurements are complicated by the unknown cluster geometries within the experimental setup. Using optimized ground-state geometries, small TiO_2 clusters have been modeled with quantum chemical methods [33], GW [34], and GW-BSE [35]. On the other hand, a recent GW study has suggested that isomers with high vertical electron affinities rather than those with the lowest ground-state energies are selectively observed in photoemission experiments performed on TiO_2 cluster anions [36]. Instead of direct comparison to experiment, some computational studies have focused on predicting trends for idealized low-dimensional nanostructures based on the bulk rutile, anatase, or brookite crystal structures. At the GW or BSE level, this includes research analyzing anatase nanosheets [37] and nanowires [38]. More of a gray area, in terms of physical relevance, is reached when the effects of dye sensitization or surrounding medium are considered. Both the details of the atomic configuration and constraints

*lhung@uic.edu
†ogut@uic.edu

on simulation size due to computational costs can affect the accuracy and applicability of the result. For instance, a common strategy for simulating excitations and charge transfer in DSSCs has been to model the substrate using finite, bulk-terminated TiO_2 fragments, either in TDDFT [39–43] or GW [44,45]. However, it may be tricky to extrapolate the behavior of a bulk DSSC from these types of calculations. Convergence of electronic properties with cluster size can be slow, and comparison of optical cluster properties with optical bulk properties (i.e., comparing the absorption cross section of a cluster with the imaginary part of the bulk dielectric function) may not be straightforward.

Motivated by the growing need for an accurate understanding of nanostructured TiO_2, here we investigate the size and shape dependence of rutile TiO_2 nanocrystals (NCs) and study trends in their electronic and optical properties. We use the GW approximation and TDDFT within a real-space framework (no periodic boundary conditions), where the single-particle wave functions are represented on a three-dimensional grid inside a spherical domain. The simulated NCs contain 2 to 64 TiO_2 units and are bulk-terminated and passivated. By modeling large clusters which are near the limit of what is currently achievable by many-body perturbation theory methods, we gauge the strength and scale of quantum confinement effects, and assess how/if the "bulk" limit is reached using clusters with more than a hundred atoms. This analysis has particular relevance to the method of using TiO_2 clusters as the substrate when modeling DSSCs, as mentioned above. Moreover, a fundamental understanding of the size and shape dependence of rutile NCs is important for the engineering of band gaps and energy levels. The rest of the paper is organized as follows. In the next section, we discuss our computational methodology, paying particular attention to the techniques that enhance the efficiency of the GW computations for these relatively large and computationally challenging transition-metal-oxide NCs. In addition to the static remainder terms used to accelerate the convergence of sums over empty states [46–49], we make use of (i) the increase in the spectral width of empty states due to the quantum confinement imposed by boundary conditions, and (ii) exponential fits to obtain converged GW energies for accurate predictions of quasiparticle levels. Results from our DFT, GW, and TDDFT calculations are presented in Sec. III along with a discussion of the size and shape dependence of the ionization potentials (IPs), electron affinities (EAs), quasiparticle gaps, and optical gaps. We also show that the overall features in the TDDFT spectra of TiO_2 NCs can be predicted quite well within the classical Mie-Gans theory using the bulk dielectric function of TiO_2. We conclude with a brief summary in Sec. IV.

II. METHODS

A. Geometry of nanocrystals

In this work, we study cuboid TiO_2 NCs with bulk rutile geometry in which the (110) and (001) surfaces are exposed. NCs are constructed using the lattice parameters of $a = 4.5937$ Å, $c = 2.9581$ Å, and $u = 0.3056$. We label each NC by integers $n_\perp \times n_\parallel \times n_\ell$, where $n_\perp$ is the number of unit cells along the $[\bar{1}10]$ direction with a repeat unit length of $a\sqrt{2}$, $n_\parallel$ is the number of unit cells along the [001] direction with a repeat unit length of c, and n_ℓ is the number of layers along [110] with a repeat unit length of $a/\sqrt{2}$. The $n_\perp \times n_\parallel \times n_\ell$ NC, therefore, contains a total of $N_{TiO_2} = 2 \cdot n_\perp \cdot n_\parallel \cdot n_\ell$ TiO_2 formula units. We consider NCs of dimensions $1 \times n_\parallel \times n_\ell$ with $n_\parallel$ and n_ℓ ranging from 1 to 4, as well as NCs of dimensions $2 \times n_\parallel \times 4$ with $n_\parallel$ ranging from 1 to 4. The dangling bonds of Ti and O atoms near the surface are passivated with pseudohydrogen atoms of fractional nuclear charge. The passivation is carried out assuming covalent bonding of Ti and O with these pseudohydrogens. Using formal charges of 4+ and 2− for Ti and O ions which are normally 6-fold and 3-fold coordinated in the bulk, respectively, this implies passivating each Ti dangling bond with a pseudohydrogen of nuclear charge $4e/3$ and each O dangling bond with a pseudohydrogen of nuclear charge $2e/3$. The largest NC considered ($2 \times 4 \times 4$) contains a total number of 320 atoms including pseudohydrogens. The atomic configurations and orientations of several NCs studied in this work are shown in Fig. 1.

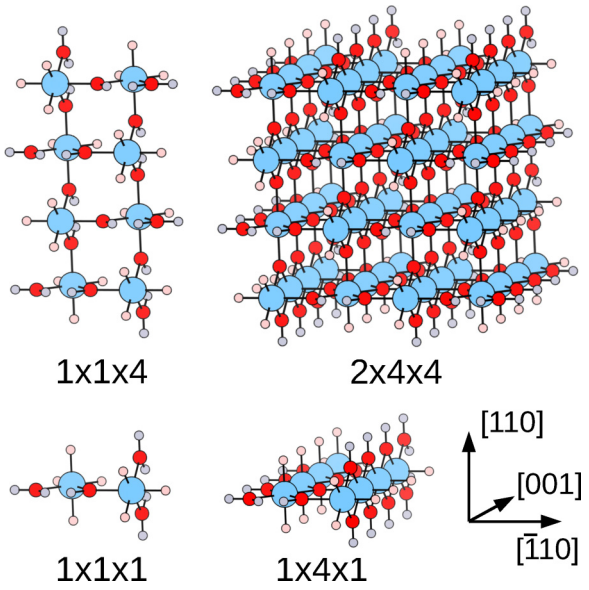

FIG. 1. (Color online) The atomic structures and orientations of the $1 \times 1 \times 1$, $1 \times 1 \times 4$, $1 \times 4 \times 1$, and $2 \times 4 \times 4$ NCs. Oxygens are red, titaniums are light blue, passivating pseudohydrogens with $4e/3$ charge are pink, and passivating pseudohydrogens with $2e/3$ charge are gray.

B. Ground-state electronic structure: Real-space Kohn-Sham DFT

We perform ground-state DFT calculations using the PARSEC code [50]. The Kohn-Sham (KS) equations are solved in real space on a uniform Cartesian grid with spacing of 0.3 a.u. The wave functions are required to vanish outside a spherical domain of radius R. Depending on both the size of the NC and the properties being studied, we use R values ranging from 12 to 36 a.u. We use the local density approximation (LDA) exchange-correlation functional of Ceperley and Alder and norm-conserving Troullier-Martins pseudopotentials [51]. The Ti pseudopotential is generated with a multireference fit [52,53] from the $3s^2 3p^6 3d^{10} 4s^2$ configuration with cutoff radii

of 1.75 a.u. for s and p angular momentum channels, and 1.65 a.u. for d. The O pseudopotential has cutoff radii of 1.45 a.u. for both s and p, while passivating pseudohydrogens have cutoff radii of 0.9 a.u. for s.

In this work, while the main purpose of KS-DFT calculations is to generate the wave functions and energies of neutral TiO_2 NCs to be used as input into higher level perturbation theory methods (TDDFT and GW), we also compute the IPs and EAs using the delta-self-consistent-field (ΔSCF) method. In this method, the IP of an n-electron system is computed from the difference in the total energy of the singly ionized system, $E(n-1)$, and the total energy of the neutral system, $E(n)$, as $\mathrm{IP}_{\Delta\mathrm{SCF}} = E(n-1) - E(n)$. Similarly, the EA is computed using the total energy of the negatively charged system, $E(n+1)$, as $\mathrm{EA}_{\Delta\mathrm{SCF}} = E(n) - E(n+1)$.

C. Electronic excitations within the GW approximation

We use the perturbative "one-shot" GW approximation (G_0W_0), where a Green's function G_0 (computed using KS wave functions) and the screened Coulomb interaction W_0 (obtained using a dynamical polarizability computed within the random phase approximation) are used to compute the self-energy, $\Sigma = iG_0W_0$. The computations are performed using the RGWBS package [46]. Dynamical effects are taken into account by summing over poles in G_0 and W_0 (full-frequency integration). To calculate the IP and EA of TiO_2 NCs within the G_0W_0 formalism, we compute the Σ matrix (including off-diagonal elements) in the basis of KS wave functions, and diagonalize. We do not include Σ matrix elements originating from the Ti $3s$, $3p$, and O $2s$ orbitals. Although these states are very important for obtaining the correct polarizability (or the dielectric function) and the Green's function, and are included for those purposes, neglecting their self-energy matrix elements alters the computed IP and EA in the diagonalized self-energy matrix by less than 1 meV. The size of the Σ matrix scales with the size of the system, ranging from 31×31 for the $1 \times 1 \times 1$ NC to 322×322 for the $1 \times 3 \times 4$ NC.

In the standard formulation of GW, a large number of unoccupied states are needed for a converged calculation. The summations over these empty states are well-known computational bottlenecks for plane-wave GW codes, and our calculations for confined systems have the same convergence properties that need to be addressed. More specifically, the GW self-energy calculation involves two sums: the first is related to the polarizability (or the dielectric function), which sums over transitions, and the second related to the Green's function G, which includes a sum over single-particle empty states. While some methods have been developed to reduce the number of empty states needed for a converged result [46–49,54,55] and others completely eliminate the need for empty states [56–58], most of these techniques have not yet seen widespread use.

In our study, convergence of the G summations is accelerated by including a "static remainder" correction term derived from the static limit of the GW approximation known as the Coulomb-hole-screened-exchange (COHSEX) approximation [46], and scaled by a factor of $1/2$ [47–49]. This correction greatly improves the convergence properties of quasiparticle levels, which is especially important when the levels have appreciable d character, as is the case for TiO_2 NCs. For example, if the static remainder is not used, even summing over 2000 unoccupied states results in an underestimate of the IP and EA by as much as 0.7 and 1.0 eV, respectively, in the relatively small $1 \times 1 \times 1$ NC. We note that here we are interested in computing the IP and EA of each NC, not just the faster-converging quasiparticle gap given by their difference. Therefore, even though the COHSEX correction improves convergence, a large number of unoccupied states must still be used to converge energies to the desired accuracy of 0.1 eV. This remains the major bottleneck as the size of the NC is increased, and we have, therefore, developed a scheme using exponential extrapolation, as summarized below, to determine the converged values for the IP and EA of TiO_2 NCs up to 24 TiO_2 units (140 atoms including pseudohydrogens resulting in a total number of 644 valence electrons). While past works have used extrapolation schemes to correct the full GW sum truncation error [16,49,59], here we apply an exponential fit to values that already include a static correction; our extrapolation accounts for errors not already treated by the COHSEX correction.

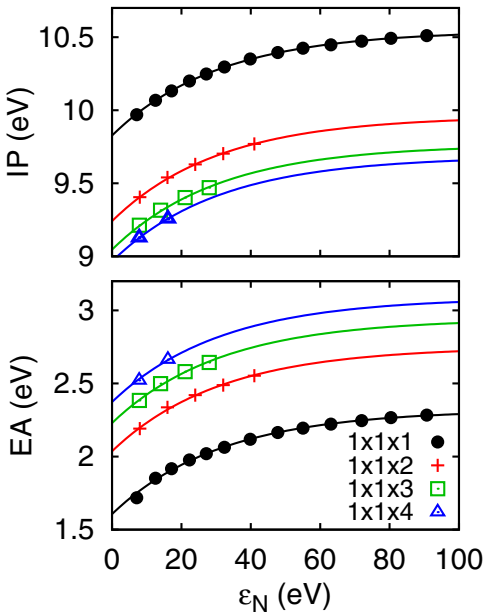

FIG. 2. (Color online) G_0W_0 IP (top) and EA (bottom) of the $1 \times 1 \times 1$ (black circles), $1 \times 1 \times 2$ (red pluses), $1 \times 1 \times 3$ (green squares), and $1 \times 1 \times 4$ (blue triangles) NCs as a function of ε_N, the KS-DFT energy of the highest state included in the Green's function summation. Exponential fits to each NC's converging quasiparticle energies are also shown.

In Fig. 2, we show the IP and EA of the $1 \times 1 \times 1$, $1 \times 1 \times 2$, $1 \times 1 \times 3$, and $1 \times 1 \times 4$ NCs at various levels of convergence, along with exponential fits to the converging G_0W_0 energies. Note that we plot the quasiparticle energies as a function of the DFT eigenvalue ε_N of the highest state N included in the sums (as elaborated further below) rather than the total number of states. We use the same cutoff for the polarizability and Green's function summations. The exponential fits to the G_0W_0 quasiparticle levels shown in

TABLE I. Information about G_0W_0 calculations used in the exponential fit for each NC. N_{data} is the number of points used in the extrapolation of the IP and EA of each NC, Min(ε_N) is the smallest summation cutoff used for a GW calculation, Max(ε_N) is the largest summation cutoff, and Max|Residual| is the largest absolute residual (difference between the data point and the exponential fit) among all IP and EA calculations for a single NC. Units are in eV.

Nanocrystal	N_{data}	Min(ε_N)	Max(ε_N)	Max|Residual|
$1\times1\times1$	13	7.1	90.7	0.032
$1\times1\times2$	5	8.0	41.0	0.016
$1\times1\times3$	4	7.9	28.0	0.013
$1\times1\times4$	2	7.8	16.1	0.010
$1\times2\times1$	13	7.2	40.0	0.042
$1\times2\times2$	3	8.0	24.0	0.012
$1\times2\times3$	2	11.3	18.9	0.010
$1\times2\times4$	1	11.7	11.7	
$1\times3\times1$	4	10.4	19.6	0.015
$1\times3\times2$	2	8.0	16.0	0.014
$1\times3\times3$	1	11.5	11.5	
$1\times3\times4$	1	8.0	8.0	
$1\times4\times1$	1	14.0	14.0	
$1\times4\times2$	1	8.0	8.0	
$1\times4\times3$	1	8.0	8.0	

Fig. 2 are of the form

$$E(\varepsilon_N) = E_{\text{conv}} - Ae^{-\varepsilon_N/B}, \quad (1)$$

where E denotes the computed quasiparticle energy (IP or EA) and the parameters E_{conv} (the converged quasiparticle energy), A, and B are determined from the fitting scheme. Using least-squares regression and weighting by ε_N, the resulting fitted parameters for the IP of the $1\times1\times1$ NC are $A_{\text{IP}} = 0.718$ eV, $B_{\text{IP}} = 30.782$ eV, and $E_{\text{conv,IP}} = 10.55$ eV. For EA of the same NC, the parameters are calculated as $A_{\text{EA}} = 0.714$ eV, $B_{\text{EA}} = 31.366$ eV, and $E_{\text{conv,EA}} = 2.32$ eV. For comparison, the most converged calculation for the $1\times1\times1$ NC (with $\varepsilon_N = 90.7$ eV) produces an IP and EA within 0.05 eV of the extrapolated converged values.

Since it is not computationally feasible to compute the GW energies of larger NCs to this level of convergence, we test whether a rigid shift of the exponential fits computed for the $1\times1\times1$ NC can represent the convergence properties of the larger NCs. In other words, parameters A_{IP}, B_{IP}, A_{EA}, and B_{EA} are fixed to the values above, and only E_{conv} is fitted for the quasiparticle energies of the other NCs. This allows us to extrapolate an estimate of the converged IP or EA for larger NCs using a manageable number of unoccupied states. We expect such fits to remain fairly accurate, since we are modeling NCs of the same underlying bulk material, which are likely to have similar behavior in the GW sum convergence. As illustrated by the exponential fits in Fig. 2 (to determine E_{conv}, while keeping the A and B parameters to the fixed values above), residuals are less than 0.04 eV for the $1\times1\times n_\ell$ NC series. Among all NCs considered, the maximum residual for the exponential fit is 0.042 eV, with smaller residuals for calculations at higher ε_N. Details about calculations used for the exponential fits for each NC are included in Table I.

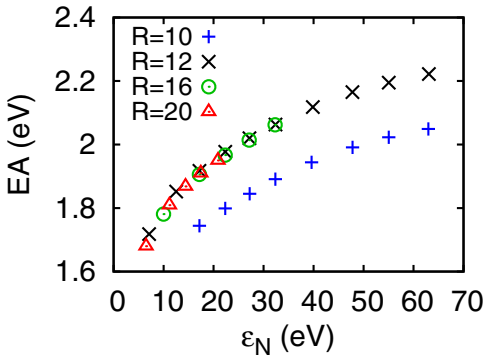

FIG. 3. (Color online) The EA of the $1\times1\times1$ NC at various levels of convergence in GW, for simulations performed in real-space cells with radii ranging from $R = 10$ to 20 a.u. The G_0W_0 EA is plotted relative to the KS-DFT energy of highest unoccupied state included in each calculation, ε_N. Results are already converged with respect to radii at $R = 12$ a.u., but not at $R = 10$ a.u., for which the predicted EA value is ~0.2 eV lower than the true EA value after achieving convergence with respect to ε_N.

We now return to our choice of converging the quasiparticle energies as a function of the DFT energy ε_N of the highest state N included in the Green's function summation. Since we use zero boundary conditions (KS wave functions required to vanish outside a spherical domain of radius R) for the confined systems studied here, the KS eigenvalues of unoccupied states at high energies are significantly affected by the choice of R. Due to quantum confinement, the spectral width of a fixed number of unoccupied states as a function of R is expected to scale approximately as R^{-2}, which we indeed find to be the case. If we held N fixed and changed R, the GW summations would extend to different maximum energies (decreasing as R increases), resulting in physically different Green's functions and polarizabilities due to the varying energy contributions. Instead, we illustrate in Fig. 3 that the appropriate comparison of GW calculations at different R is not given by calculations with the same N, but instead by calculations that include summations over all empty states up to the state with some predetermined DFT eigenvalue ε_N. Figure 3 shows the convergence properties for the EA of the $1\times1\times1$ NC computed within the G_0W_0 approximation. As a function of ε_N, the computed EAs for $R = 12$,16, and 20 a.u. all give the same GW energies, demonstrating that GW calculations are converged relative to simulation cell size. The results shown for $R = 10$ a.u. in Fig. 3, on the other hand, are significantly different from the rest of the computed EA values and converge to a different value as a function of ε_N, stemming from the fact that the DFT eigenvalue of the LUMO of the $1\times1\times1$ NC is not well converged at $R = 10$ a.u. as a function of R. Similar convergence properties are observed for the IP, and in general, our tests show that as long as R is chosen sufficiently large so that the KS eigenvalues of the relevant states (e.g., the highest occupied molecular orbital, HOMO, and the lowest unoccupied molecular orbital, LUMO, for the computations of IP and EA, respectively) are converged, the size of the simulation cell does not affect the computed quasiparticle energies.

This independence of IP and EA values with respect to the choice of R can be exploited, so that one can choose the *smallest* possible simulation cell for which HOMO and LUMO are converged at the DFT level. The benefits of a small R are twofold: First, the number of grid points, N_{grid}, in the physical domain is decreased ($N_{\text{grid}} \propto R^3$). Therefore, all Coulomb integrals, which scale as $N_{\text{grid}} \log N_{\text{grid}}$, are evaluated more quickly. Second, and more importantly, the confining smaller sphere means that fewer unoccupied states are needed to reach a given summation cutoff energy due to the quantum confinement of the simulation cell (also scaling approximately as R^3). In the specific example of the $1 \times 1 \times 1$ NC, a GW calculation with $\varepsilon_N = 20$ eV for $R = 20, 16$, and 12 a.u. requires 943, 516, and 239 states, respectively, which underscores the tremendous computational savings that quantum confinement enables in GW computations of confined nanostructures. In our G_0W_0 calculations, we use the smallest R values needed to converge KS-DFT energy levels for the states of interest, and the cell sizes for NCs up to 24 TiO_2 units accordingly range from $R = 12$ to 20 a.u.

One can provide a physical explanation for why the seemingly artificial increase in the spectral width of the unoccupied states does not have an effect on the computed IP and EA of the system. Using zero boundary conditions for a confined system essentially means that the external DFT potential $V_{\text{ext}}(\mathbf{r})$ that the valence electrons feel has, in addition to the usual ionic potential modeled by pseudopotentials $V_{\text{ion}}^{\text{ps}}(\mathbf{r})$, an extra infinite-potential term, so that

$$V_{\text{ext}}(\mathbf{r}) = \begin{cases} V_{\text{ion}}^{\text{ps}}(\mathbf{r}), & r < R, \\ \infty, & r > R, \end{cases} \tag{2}$$

constrains *all* KS eigenfunctions to vanish for $r > R$. This extra infinite potential beyond R clearly has no effect on eigenvalues or eigenfunctions of the localized occupied (and some of the low-lying unoccupied) KS states as long as R is sufficiently large, which is one of the routine convergence tests that we perform using PARSEC for any confined system. Higher-lying unoccupied states, on the other hand, are affected by this infinite potential term such that their spectral width increases significantly. However, the set of eigenfunctions that correspond to the solutions of the KS equations with this modified $V_{\text{ext}}(\mathbf{r})$ still form a complete, orthonormal set of single-particle states that can act as a basis. The advantage of using a basis of such KS eigenfunctions is that at a fixed number of single-particle states used in GW summations, they span a much wider energy range. In other words, the higher-energy empty states are used to produce as complete a basis as possible in the relevant space, and not so much for their physical meaning. Localized Kohn-Sham states have already been used to accelerate GW sums over empty states, in conjunction with a plane-wave formalism [60], and the fact that higher-energy wave functions do not need to be physical can be seen as a confined-system analog of the technique of simply using plane waves as empty states in GW sums [61]. From a physical perspective, this means that the IP and EA values obtained from direct or inverse photoemission experiments performed on "truly isolated" nanostructures, and hypothetical experiments performed on nanostructures constrained in "artificial" rigid boxes of large enough radii R, will be the same. With such apparent freedom in the form of these higher-energy states, further study of localized, quantum-confined empty states may aid future development of efficient GW algorithms.

D. Optical excitations within TDDFT

In this work, the optical excitations for all NCs are calculated via TDDFT using the adiabatic LDA exchange correlation functional (TDLDA). We use Casida's frequency domain formalism as implemented in the RGWBS software suite [46,62]. Because TDLDA models excitations to more diffuse states, larger simulation cells are needed here for converged calculations compared to GW calculations. For TDLDA calculations, our simulation cell radii range from $R = 20$ to 36 a.u. The resulting absorption spectra are converged with a resolution of 0.1 eV for frequencies up to ~8 eV, and demonstrate the general trends in line shapes for the 8–10 eV range.

The TDLDA spectra are used to estimate the optical band gaps for various NCs, but a quantitative comparison of the optical gaps is complicated by the gradual onset of the optical edge. TDLDA calculations for most NCs predict multiple low-energy transitions with very low oscillator strengths, which would be too weak to be detected in experiments. Therefore, following the approach in previous studies [63,64], we define the optical band gap $E_{\text{opt}}(p)$ to be the energy at which the integrated oscillator strength reaches a certain threshold p. In terms of the photoabsorption cross section $\sigma(\omega)$, this means that $E_{\text{opt}}(p)$ is defined as

$$\int_0^{E_{\text{opt}}(p)} \sigma(\omega) d\omega = p f_e, \tag{3}$$

where $f_e = 2\pi^2 \hbar e^2 / mc = 1.098$ eV Å^2 is the complete one-electron oscillator strength, and p is proportion of oscillator strength chosen as the threshold to define the gap. In previous studies, the optical gap was defined at $p = 0.02$, which we also choose as our threshold. However, since the intensity of the absorption cross section is proportional to cluster size, we also present a comparison to a scaled threshold, $p_{\text{scaled}} = N_{\text{TiO}_2} \times 10^{-4}$.

III. RESULTS AND DISCUSSION

A. Quasiparticle energy levels

The IPs and EAs of rutile TiO_2 NCs are computed using the ΔSCF and G_0W_0 methods for NCs up to 64 and 24 TiO_2 units, respectively. We first focus on the effect of quantum confinement on the NC energy levels. Figure 4 shows the IPs and EAs as a function of N_{TiO_2}. For NCs with the same N_{TiO_2} but with different shapes, we show the average of their computed values. In addition to the ΔSCF and G_0W_0 values, the corresponding KS-DFT values (negative of HOMO and LUMO energies) are also shown. At the KS-DFT level, quantum confinement is barely observed. EAs remain ~4.6 eV, and IPs vary less than 0.5 eV from $N_{\text{TiO}_2} = 4$ to 64. At the ΔSCF and G_0W_0 levels, on the other hand, there is a clear size dependence, with larger NCs closer to bulk energy levels, and small NCs having quasiparticle gaps >8 eV. Neither G_0W_0 nor ΔSCF quasiparticle energies can be described as a rigid shift from KS-DFT eigenvalues. Hence, while KS-DFT

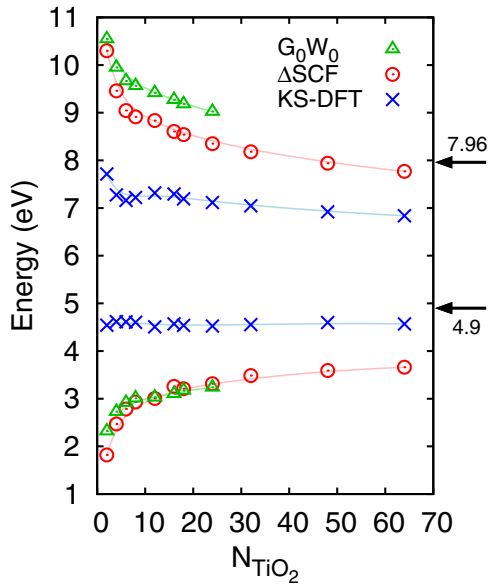

FIG. 4. (Color online) Comparison of IPs (above 6 eV) and EAs (below 6 eV) as a function of the number of TiO_2 units in the NC, calculated at three levels of theory: G_0W_0 (green triangles), ΔSCF (red circles), and KS-DFT (blue crosses). For values of N_{TiO_2} that correspond to more than one NC, the average value is plotted. Experimental bulk levels of 7.96 eV and 4.9 eV for IP and EA, respectively, are indicated by arrows at the right. Lines are a guide for the eye.

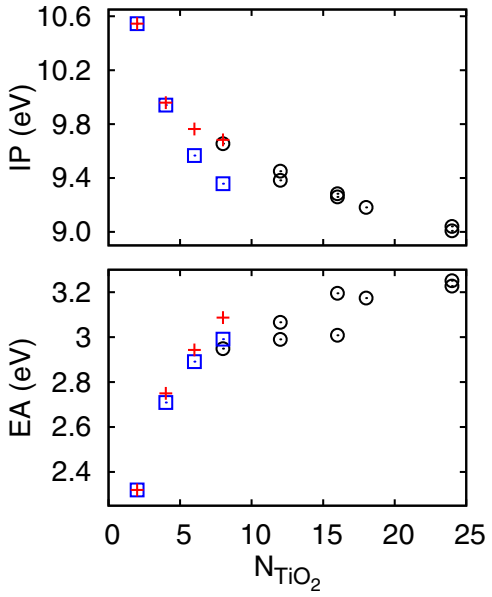

FIG. 5. (Color online) IPs (top) and EAs (bottom) predicted by G_0W_0 as a function of N_{TiO_2}. Quasiparticle energies of the $1 \times n_{\|} \times 1$ series are indicated by blue squares, the $1 \times 1 \times n_{\ell}$ NC series by red pluses, and the remaining NCs by black circles. All G_0W_0 quasiparticle energies are also listed in Table II.

theory predicts some size-dependence, the relative energies of different NCs cannot be used to predict energy levels and band gaps, and a simple scissor operator (shifting all KS-DFT band gaps by the same value) does not allow KS-DFT to reproduce size-dependent effects quantitatively.

The ΔSCF calculations are expected to decrease in accuracy for larger calculations, due to increasing delocalization errors and incorrect asymptotic behavior of the LDA functional. We expect greater accuracy and consistency from the G_0W_0 computations. When comparing between G_0W_0 and ΔSCF predictions, we observe that the difference between the two methods is roughly constant for NCs with 8 to 24 TiO_2 units. While the ΔSCF and G_0W_0 predictions for EA in this size range are nearly the same (within $\sim$0.1 eV of each other), ΔSCF consistently underestimates the IP by $\sim$0.65 eV compared to G_0W_0. Very similar trends with respect to ΔSCF and GW predictions were observed for Si NCs as a function of size [46].

For the smallest NC, G_0W_0 predicts IP and EA offsets from bulk values that are close in magnitude, with the IP 2.59 eV higher than the bulk rutile IP of 7.96 eV, and the EA 2.58 eV lower than the bulk EA of 4.9 eV [65,66]. With respect to the rate at which the bulk limit is approached, however, there seems to be an appreciable difference between the IP and the EA. We now consider the $2 \times 4 \times 4$ NC, which is the largest in our study with an average linear dimension of $\sim$1.46 nm. Assuming that the G_0W_0 prediction is still offset by 0.65 eV from the ΔSCF value for this NC, its IP would be 8.42 eV, which is within 0.5 eV of the bulk limit. On the other hand, the predicted EA at this size range would be 3.66 eV, more than 1.2 eV below the bulk limit (using the ΔSCF value directly as our estimate, since ΔSCF values are very close to the G_0W_0 values for smaller NCs). We speculate that this difference in convergence rates is due to differences in the orbital characters of the HOMO and the LUMO of the NCs (or equivalently, the valence band maximum and the conduction band minimum of bulk TiO_2) which have primarily O $2p$ and Ti $3d$ characters, respectively.

In Fig. 5, we plot the G_0W_0 IPs and EAs for TiO_2 NCs, which exhibit a considerable shape dependence. The EA of the $1 \times 2 \times 4$ NC is $\sim$0.2 eV greater than that of the $1 \times 4 \times 2$ NC, and the IP of the $1 \times 1 \times 4$ NC is more than 0.3 eV greater than that of the $1 \times 4 \times 1$ NC. In fact, comparing the IPs for the $1 \times 1 \times n$ and the $1 \times n \times 1$ series, which are effectively two-dimensional NCs with predominantly (001) and (110) surfaces exposed (see Fig. 1), respectively, we see that the shape dependence becomes more significant as n increases. These findings suggest that the quasiparticle levels of TiO_2 NCs can be tuned at least on the order of tenths of eV's by manipulating their shapes. For shape-dependent properties of TiO_2 NCs, we again caution against trusting trends at the KS-DFT level: The shape dependence observed via G_0W_0 (and ΔSCF) is significantly diminished relative to the shape dependence observed in KS-DFT. An extreme example compares the $1 \times 2 \times 1$ and $1 \times 1 \times 2$ NCs, which differ by 0.31 eV according to KS-DFT, 0.08 eV according to ΔSCF, and 0.02 eV according to G_0W_0. Energy orderings for NCs with the same N_{TiO_2} can also shift when going from KS-DFT to higher levels of theory. However, we find that the ΔSCF and G_0W_0 energies generally predict the same trends. A full comparison of eigenvalues at the KS-DFT, ΔSCF, and G_0W_0 levels is available in Table II.

TABLE II. Gaps, IPs, and EAs from KS-DFT, TDLDA, G_0W_0, and ΔSCF. Expected accuracy of values is ∼0.1 eV.

Cluster	$\text{Gap}_{\text{TDLDA}}$	IP_{KSDFT}	EA_{KSDFT}	$\text{IP}_{\Delta\text{SCF}}$	$\text{EA}_{\Delta\text{SCF}}$	IP_{GW}	EA_{GW}
1 × 1 × 1	3.60	7.71	4.54	10.30	1.82	10.55	2.32
1 × 1 × 2	3.30	7.43	4.63	9.50	2.52	9.96	2.75
1 × 1 × 3	2.94	7.40	4.64	9.18	2.85	9.76	2.94
1 × 1 × 4	2.83	7.40	4.66	8.96	3.08	9.68	3.09
1 × 2 × 1	3.59	7.12	4.61	9.42	2.42	9.94	2.71
1 × 2 × 2	3.28	7.44	4.56	9.20	2.80	9.66	2.95
1 × 2 × 3	3.08	7.27	4.56	8.83	3.07	9.38	3.07
1 × 2 × 4	3.03	7.21	4.60	8.61	3.27	9.26	3.20
1 × 3 × 1	3.30	6.93	4.59	8.91	2.72	9.57	2.89
1 × 3 × 2	3.28	7.36	4.45	8.84	2.94	9.45	2.99
1 × 3 × 3	3.11	7.19	4.54	8.54	3.21	9.18	3.17
1 × 3 × 4	2.94	7.12	4.53	8.38	3.31	9.04	3.25
1 × 4 × 1	3.11	6.83	4.58	8.58	2.91	9.36	2.99
1 × 4 × 2	3.05	7.29	4.41	8.62	3.05	9.28	3.01
1 × 4 × 3	3.01	7.11	4.52	8.32	3.32	9.01	3.23
1 × 4 × 4	2.89	7.05	4.49	8.19	3.40		
2 × 1 × 4	2.79	7.39	4.71	8.59	3.46		
2 × 2 × 4	2.87	7.05	4.62	8.17	3.57		
2 × 3 × 4	2.80	6.92	4.60	7.94	3.59		
2 × 4 × 4	2.75	6.84	4.57	7.77	3.66		

B. Optical and quasiparticle gaps

The absorption cross sections of all 20 NCs predicted via TDLDA are shown in Fig. 6. All spectra share the common features of a small peak near 5 eV and significantly increasing oscillator strengths starting at ∼8 eV. The small peak shifts to slightly higher energies upon increase of the NC size. Smaller NCs have widely spaced discrete states and therefore more oscillations in the overall line shape, while the largest NCs have much smoother spectra.

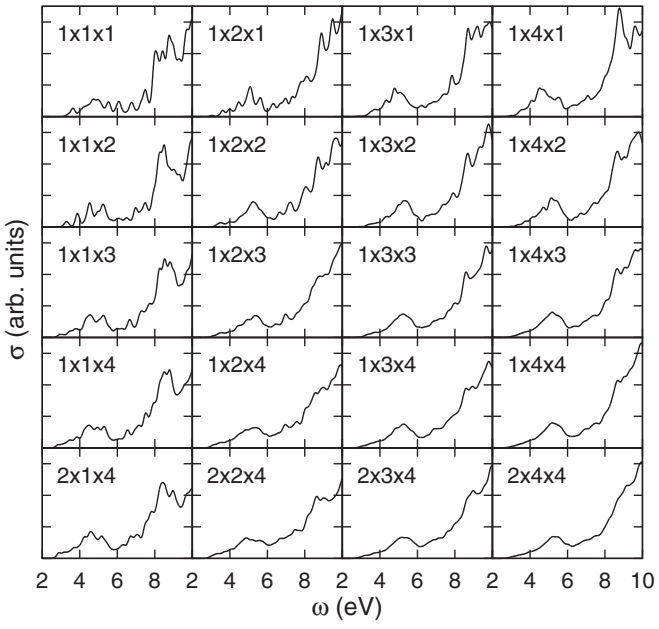

FIG. 6. TDLDA absorption cross sections for TiO_2 NCs as a function of energy. The spectra are scaled by N_{TiO_2} for easier comparison of features. Spectra have a Gaussian broadening of 0.1 eV.

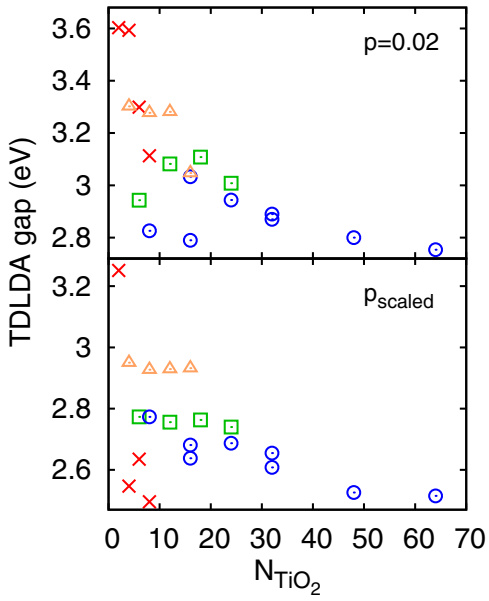

FIG. 7. (Color online) TDLDA optical gaps evaluated with an absolute threshold $p = 0.02$ (top) and with a scaled threshold $p_{\text{scaled}} = N_{TiO_2} \times 10^{-4}$ (bottom). The red crosses correspond to NCs with $n_\ell = 1$, the orange triangles to NCs with $n_\ell = 2$, the green squares to NCs with $n_\ell = 3$, and the blue circles to NCs with $n_\ell = 4$. All TDLDA gaps for $p = 0.02$ are also included in Table II.

A comparison of TDLDA optical gaps for various NCs, defined at two different thresholds ($p = 0.02$ and $p_{\text{scaled}} = N_{TiO_2} \times 10^{-4}$), is shown in Fig. 7. While most trends in size and shape dependence remain consistent between the two choices of the threshold, the predicted optical gaps and ordering of optical gaps do have some sensitivity to the threshold criterion, which serves as a reminder that the definition of the optical gap is important when comparing reported values, whether measured experimentally or simulated theoretically.

As a result of quantum confinement, the TDLDA optical gaps increase when the sizes of the NCs decrease, just like the quasiparticle gaps. The absorption edge onsets range from 2.75 to 3.60 eV ($p = 0.02$) or from 2.52 to 3.25 eV ($p_{\text{scaled}} = N_{TiO_2} \times 10^{-4}$) for NCs with 64 to 2 TiO_2 units. The TDLDA gaps also exhibit shape dependence, with optical gaps for NCs of the same size varying up to ∼0.4 eV. The amount of each surface exposed in the two NCs [(110) versus (001)] is again a likely cause for these differences. For both thresholds, we observe that the optical gap depends primarily on n_ℓ once we move beyond the monolayer NCs. This is especially clear with optical gaps defined at the p_{scaled} threshold. Apart from the monolayer NCs, the remaining $n_\perp \times n_\parallel \times 2$ NCs all have TDLDA gaps in the range 2.9–3.0 eV, the $n_\perp \times n_\parallel \times 3$ NCs have TDLDA gaps of 2.7–2.8 eV, and the $n_\perp \times n_\parallel \times 4$ NCs have TDLDA gaps of 2.5–2.7 eV. TDLDA optical gaps defined at the threshold $p = 0.02$ are also included in Table II.

In Fig. 8, we compare the size dependence of (shape-averaged) TDLDA optical gaps ($p = 0.02$) with ΔSCF and G_0W_0 quasiparticle gaps from the previous section. The quantum confinement effects reflected in the quasiparticle gaps are observed to persist in the largest NCs simulated. Even for the 2 × 4 × 4 NC (64 TiO_2 units), the ΔSCF quasiparticle gap

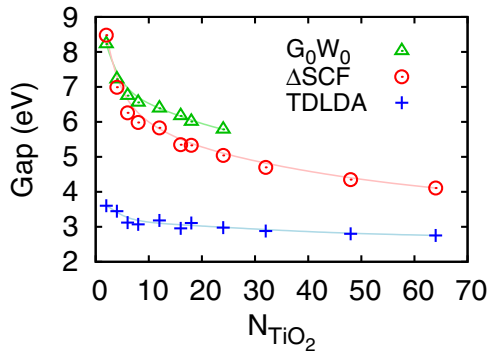

FIG. 8. (Color online) Quasiparticle gaps at the ΔSCF (red circles) and G_0W_0 (green triangles) levels, and optical gaps inferred from TDLDA absorption spectra with $p = 0.02$ threshold (blue pluses) as a function of N_{TiO_2}. At a given size, the values for NCs differing in shape are averaged. Lines are a guide for the eye.

remains more than 1 eV larger than that of the bulk, and trends suggest that the corresponding G_0W_0 gap would be even larger. The TDLDA optical gaps have a weaker size dependence compared to quasiparticle gaps at either level of theory. The difference between the quasiparticle gap and the optical gap gives the exciton binding energy E_b, i.e., the magnitude of the electron-hole interaction. Using the computed G_0W_0 quasiparticle and TDLDA optical gaps, we find E_b values ranging from 4.6 eV ($N_{TiO_2} = 2$) to 2.0 eV ($N_{TiO_2} = 64$). These exciton binding energies are much larger than the estimates for bulk exciton binding energies near or less than 0.1 eV [15,16], and are comparable in magnitude to excitonic effects predicted for stoichiometric TiO_2 clusters [35]. We note that the TDLDA optical gap predicted for the largest NC is already below the experimental bulk optical gap near 3.0 eV. This is not surprising, since we expect the $N_{TiO_2} \to \infty$ (bulk) limit of TDLDA optical gaps to be the KS-DFT band gap near 1.8 eV. More accurate treatment within the *GW*-BSE formalism is likely to shift the optical gaps up by ∼1 eV compared to the TDLDA values [35], but we still expect the overall trend of significantly enhanced exciton binding energies to remain valid in the quantum-confined NCs, especially if we focus on the smaller NCs ($N_{TiO_2} < 10$) where we expect TDLDA optical gaps to be more reliable.

C. Quantum and classical absorption spectra

In the previous sections, we have shown that the quasiparticle energies and gaps of the largest ($2 \times 4 \times 4$) NC with 64 TiO_2 are still not converged to the bulk limit. The TDDFT spectra displayed in Fig. 6 do not resemble the imaginary part of the bulk rutile dielectric function, $\epsilon_2(\omega)$, even for the largest NC considered (after accounting for anisotropies and scaling by energy). In light of these observations, it is, therefore, important to investigate the connection between the optical properties of bulk TiO_2 and TDLDA spectra of nm-sized bulk-truncated NCs in an effort to understand if and how the latter can be used to represent the former.

In recent studies [67–69], some of us showed that the TDDFT absorption spectra of small Si_n, Ag_n, and Cu_n clusters in the intermediate-size regime ($10 < n < 30$) can be reproduced remarkably well using the Mie-Gans theory [70–72]. In Mie-Gans theory, the absorption cross section of an ellipsoidal nanoparticle smaller than the wavelength of light is obtained from the bulk dielectric function as a solution of Maxwell's equations. That the bulk dielectric function of the constituent element can be used to predict the optical absorption spectra of such small systems in the *subnanometer* scale using a classical theory is a finding which has motivated us to investigate whether similar observations can be made for the case of TiO_2 NCs.

The Mie-Gans absorption cross section σ_{MG} for an ellipsoidal cluster with volume V and depolarization factors G_i is given by

$$\sigma_{MG}(\omega) = \frac{V\omega}{3c} \sum_{i=1}^{3} \frac{\epsilon_{2,i}(\omega)}{\{1 + G_i[\epsilon_{1,i}(\omega) - 1]\}^2 + [G_i\epsilon_{2,i}(\omega)]^2}, \tag{4}$$

where c is the speed of light, $i = x,y,z$ is the index for the Cartesian direction, and $\epsilon_{1,i}$ and $\epsilon_{2,i}$ are the real and imaginary parts of the ith component of the dielectric tensor of the bulk material, respectively. In the above equation, the ellipsoid axes are assumed to be aligned with the principal axes of the dielectric tensor, which is the case in our work, given the crystal structure of rutile TiO_2 and the particular cuboid geometry of the NCs considered. The depolarization factors G_i satisfy $\sum_{i=1}^{3} G_i = 1$ and are related to the proportions of the ellipsoid [72]. For example, a sphere has $G_1 = G_2 = G_3 = 1/3$, a prolate (cigar-shaped) ellipsoid has $G_1 < G_2 = G_3$, and an oblate ellipsoid (pancake-shaped) has $G_1 = G_2 < G_3$. To compute the depolarization factors G_i for each NC, we first identify the smallest ellipsoid containing all atoms centers (including passivating pseudo-hydrogens). Using the dimensions of this ellipsoid, we can directly calculate the depolarization factors by means of the relevant elliptic integrals, as given in Ref. [73]. In generating the Mie-Gans spectra, we use the bulk rutile TiO_2 dielectric functions from G_0W_0 calculations performed by Landmann *et al.*, which show good agreement with experiment, but are available to higher energies [17,74].

In Fig. 9, we show the Mie-Gans spectra together with TDLDA spectra of the smallest ($1 \times 1 \times 1$) and largest ($2 \times 4 \times 4$) NCs simulated in this work. Here, we have blueshifted the TDLDA spectra by ∼1 eV in order to align the small peak positions predicted near 5 and 6 eV by TDLDA and Mie-Gans theory, respectively. This empirical shift is done to compare the overall features of the predictions from the two approaches, and can be justified, to some extent, in terms of the well-known underestimate of absorption edge onsets within TDLDA in comparison to more accurate treatments such as *GW*-BSE [35]. The agreement between the Mie-Gans and TDLDA predictions is quite good in terms of the overall shape characterized by a small peak near 6 eV and the significant rise in the absorption cross section beyond 9 eV for both the smallest and the largest NCs considered.

Our findings in earlier studies on Si_n, Ag_n, and Cu_n clusters combined with the present results for the case of more complex (in terms of size, composition, and anisotropic nature) TiO_2 NCs show that Mie-Gans theory can accurately account for the absorption spectra of (sub)nanometer-sized clusters. Even though the quasiparticle levels of even the

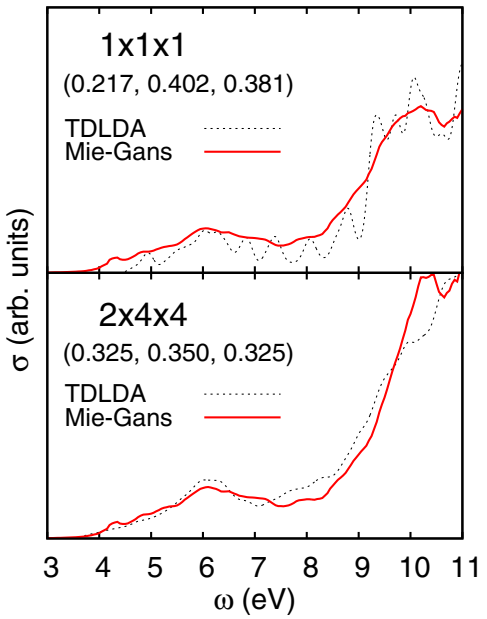

FIG. 9. (Color online) TDLDA versus Mie-Gans optical spectra for the $1 \times 1 \times 1$ (top) and $2 \times 4 \times 4$ (bottom) NCs. The depolarization factors used to compute the Mie-Gans spectra for the NCs are given in each figure.

largest NC considered here have not yet reached the bulk limit and its absorption cross section does not resemble the imaginary part of the bulk dielectric function with its well-defined Van Hove singularities, we observe that the "concept" of bulk dielectric function still survives to the (sub)nanometer-size regime. As suggested earlier by Tiago and Chelikowsky [75], the absorption cross section $\sigma(\omega)$ of a (sub)nanometer-sized NC, such as the ones considered here, is primarily dominated by Mie surface plasmons due to the finite size of the system that is much smaller than the wavelength of the electromagnetic field. However, it is possible to connect $\sigma(\omega)$ of a nanoparticle to the bulk dielectric function through a nonlinear Clausius-Mosotti-like relationship, of which the Mie-Gans expression in Eq. (4) is a specialized case extended to anisotropic ellipsoids. Therefore, our results for both the electronic and optical excitations in TiO_2 NCs suggest that one should exercise caution in modeling the electronic and optical properties of macroscale TiO_2 particles via the use of small passivated TiO_2 NCs and extrapolating the results from the latter idealized systems to practically bulklike length scales.

IV. SUMMARY

We use the GW approximation and TDLDA, implemented in real space, to examine the electronic properties and optical excitations in bulk-terminated rutile TiO_2 nanocrystals. In terms of methodology, we focus on techniques that reduce the computational cost of the most expensive step of this work: the sum-over-empty-states bottleneck in GW. Some of these methods, such as the COHSEX static remainder and exponential extrapolation, can be applied to both confined and extended systems. However, other significant gains in GW efficiency are only possible when modeling localized wave functions, like those of the TiO_2 NCs in this study. In our real-space implementation, we demonstrate that once a simulation cell is large enough that the occupied (and certain bound, low-lying unoccupied) states are not affected by the finite cell size, the converged GW energies of such states are also unaffected by the finite cell size. The increased spectral width of the high-lying unoccupied orbitals in the relatively small confined simulation cells reduces the number of empty states needed to converge a GW calculation. Together, these various theories and approximations allow us to predict the IPs and EAs (and not just the quasiparticle gaps) of TiO_2 NCs using G_0W_0.

The IP and EA computed with G_0W_0 are compared to those determined via ΔSCF, and EA values agree fairly well between the two theories. However, the IPs of ΔSCF are consistently smaller than those of G_0W_0. Size and shape dependence are observed for both optical and electronic excitations in the NCs. NCs of the same size, but different shape, have G_0W_0 quasiparticle energies differing up to 0.3 eV and optical gaps differing up to 0.4 eV. These results suggest that the anisotropies in TiO_2 nanostructures could be used to engineer desired electronic and optical properties by tuning their shape. The largest clusters modeled via G_0W_0, containing 24 TiO_2 formula units, are found to have quasiparticle gaps of 4.2 eV, $\sim$1 eV larger than the bulk gap, while the smallest NC has a quasiparticle gap of 8.2 eV. The optical gaps, as determined via TDLDA, vary from 2.8 to 3.6 eV. While we do expect these TDLDA results to underestimate the true optical gaps, it still appears that the quasiparticle levels are more sensitive to quantum confinement than optical gaps.

Even for the largest NCs simulated in this study (24 TiO_2 units for G_0W_0 and 64 for ΔSCF and TDLDA), the IPs, EAs, and optical gaps have not yet converged to their bulk values. Continued research to further improve the efficiency of many-body perturbation theory methods is still necessary before we can bridge the scales from confined systems to bulk. In the meantime, cluster methods often used in modeling DSSCs must be carefully evaluated if they are used to study dye-sensitized bulk. However, we show that the concept of the bulk dielectric function still survives down to (sub)nanometer length scale in an interesting way: Given the anisotropic bulk dielectric function, the classical Mie-Gans theory can reproduce fairly accurately the TDLDA spectral features for the full range of NCs considered in this study.

ACKNOWLEDGMENTS

This work was supported by U.S. Department of Energy Grant No. DE-FG02-09ER16072, and used resources of the National Energy Research Scientific Computing Center, a DOE Office of Science User Facility supported by the Office of Science of the U.S. Department of Energy under Contract No. DE-AC02-05CH11231.

[1] A. Fujishima, X. Zhang, and D. A. Tryk, Surf. Sci. Rep. **63**, 515 (2008).

[2] M. Grätzel, Nature (London) **414**, 338 (2001).

[3] A. Hagfeldt, G. Boschloo, L. Sun, L. Kloo, and H. Pettersson, Chem. Rev. **110**, 6595 (2010).
[4] X. Chen and S. S. Mao, Chem. Rev. **107**, 2891 (2007).
[5] L. Liu and X. Chen, Chem. Rev., **114** 9890 (2014).
[6] L. Sang, Y. Zhao, and C. Burda, Chem. Rev., **114**, 9283 (2014).
[7] N. Satoh, T. Nakashima, K. Kamikura, and K. Yamamoto, Nat. Nanotechnol. **3**, 106 (2008).
[8] N. Serpone, D. Lawless, and R. Khairutdinov, J. Phys. Chem. **99**, 16646 (1995).
[9] S. Monticone, R. Tufeu, A. V. Kanaev, E. Scolan, and C. Sanchez, Appl. Surf. Sci. **162–163**, 565 (2000).
[10] H.-J. Zhai and L.-S. Wang, J. Am. Chem. Soc. **129**, 3022 (2007).
[11] L. Vayssieres, C. Persson, and J.-H. Guo, Appl. Phys. Lett. **99**, 183101 (2011).
[12] F. De Angelis, C. Di Valentin, S. Fantacci, A. Vittadini, and A. Selloni, Chem. Rev. **114**, 9708 (2014).
[13] C. Sousa, S. Tosoni, and F. Illas, Chem. Rev. **113**, 4456 (2013).
[14] Y. Ping, D. Rocca, and G. Galli, Chem. Soc. Rev. **42**, 2437 (2013).
[15] L. Chiodo, J. M. García-Lastra, A. Iacomino, S. Ossicini, J. Zhao, H. Petek, and A. Rubio, Phys. Rev. B **82**, 045207 (2010).
[16] W. Kang and M. S. Hybertsen, Phys. Rev. B **82**, 085203 (2010).
[17] M. Landmann, E. Rauls, and W. G. Schmidt, J. Phys.: Condens. Matter **24**, 195503 (2012).
[18] H. Peng and J. Li, J. Phys. Chem. C **112**, 20241 (2008).
[19] A. Iacomino, G. Cantele, F. Trani, and D. Ninno, J. Phys. Chem. C **114**, 12389 (2010).
[20] T. He, Z. S. Hu, J. L. Li, and G. W. Yang, J. Phys. Chem. C **115**, 13837 (2011).
[21] A. Hmiel and Y. Xue, Phys. Rev. B **85**, 235461 (2012).
[22] R. A. Evarestov and Y. F. Zhukovskii, Surf. Sci. **608**, 226 (2013).
[23] Z.-w. Qu and G.-J. Kroes, J. Phys. Chem. C **111**, 16808 (2007).
[24] A. Iacomino, G. Cantele, D. Ninno, I. Marri, and S. Ossicini, Phys. Rev. B **78**, 075405 (2008).
[25] H. Peng, J. Li, S.-S. Li, and J.-B. Xia, J. Phys. Chem. C **112**, 13964 (2008).
[26] S. K. Sahoo, S. Pal, P. Sarkar, and C. Majumder, Chem. Phys. Lett. **516**, 68 (2011).
[27] D. Çakır and O. Gülseren, J. Phys.: Condens. Matter **24**, 305301 (2012).
[28] V. C. Fuertes, C. F. A. Negre, M. B. Oviedo, F. P. Bonafé, F. Y. Oliva, and C. G. Sánchez, J. Phys.: Condens. Matter **25**, 115304 (2013).
[29] S. A. Shevlin and S. M. Woodley, J. Phys. Chem. C **114**, 17333 (2010).
[30] S. Auvinen, M. Alatalo, H. Haario, J.-P. Jalava, and R.-J. Lamminmäki, J. Phys. Chem. C **115**, 8484 (2011).
[31] M. Gałyńska and P. Persson, Int. J. Quantum Chem. **113**, 2611 (2013).
[32] E. Berardo, H.-S. Hu, S. A. Shevlin, S. M. Woodley, K. Kowalski, and M. A. Zwijnenburg, J. Chem. Theory Comput. **10**, 1189 (2014).
[33] S. Li and D. A. Dixon, J. Phys. Chem. A **112**, 6646 (2008).
[34] D. J. Mowbray, J. I. Martinez, J. M. García Lastra, K. S. Thygesen, and K. W. Jacobsen, J. Phys. Chem. C **113**, 12301 (2009).
[35] L. Chiodo, M. Salazar, A. H. Romero, S. Laricchia, F. D. Sala, and A. Rubio, J. Chem. Phys. **135**, 244704 (2011).
[36] N. Marom, M. Kim, and J. R. Chelikowsky, Phys. Rev. Lett. **108**, 106801 (2012).
[37] M. Palummo, G. Giorgi, L. Chiodo, A. Rubio, and K. Yamashita, J. Phys. Chem. C **116**, 18495 (2012).
[38] H. Ünal, O. Gülseren, Ş. Ellialtıoğlu, and E. Mete, Phys. Rev. B **89**, 205127 (2014).
[39] M. Makowska-Janusik, O. Gladii, A. Kassiba, J. Bouclé, and N. Herlin-Boime, J. Phys. Chem. C **118**, 6009 (2014).
[40] T. Le Bahers, T. Pauporté, P. P. Lainé, F. Labat, C. Adamo, and I. Ciofini, J. Phys. Chem. Lett. **4**, 1044 (2013).
[41] R. Sánchez-de-Armas, J. Oviedo López, M. A. San-Miguel, J. F. Sanz, P. Ordejón, and M. Pruneda, J. Chem. Theory Comput. **6**, 2856 (2010).
[42] S. Meng, J. Ren, and E. Kaxiras, Nano Lett. **8**, 3266 (2008).
[43] F. De Angelis, A. Tilocca, and A. Selloni, J. Am. Chem. Soc. **126**, 15024 (2004).
[44] N. Marom, J. E. Moussa, X. Ren, A. Tkatchenko, and J. R. Chelikowsky, Phys. Rev. B **84**, 245115 (2011).
[45] N. Marom, T. Körzdörfer, X. Ren, A. Tkatchenko, and J. R. Chelikowsky, J. Phys. Chem. Lett. **5**, 2395 (2014).
[46] M. L. Tiago and J. R. Chelikowsky, Phys. Rev. B **73**, 205334 (2006).
[47] W. Kang and M. S. Hybertsen, Phys. Rev. B **82**, 195108 (2010).
[48] J. Deslippe, G. Samsonidze, M. Jain, M. L. Cohen, and S. G. Louie, Phys. Rev. B **87**, 165124 (2013).
[49] J. Klimeš, M. Kaltak, and G. Kresse, Phys. Rev. B **90**, 075125 (2014).
[50] L. Kronik, A. Makmal, M. L. Tiago, M. M. G. Alemany, M. Jain, X. Huang, Y. Saad, and J. R. Chelikowsky, Phys. Status Solidi B **243**, 1063 (2006).
[51] N. Troullier and J. L. Martins, Phys. Rev. B **43**, 1993 (1991).
[52] C. L. Reis, J. M. Pacheco, and J. L. Martins, Phys. Rev. B **68**, 155111 (2003).
[53] M. J. T. Oliveira and F. Nogueira, Comput. Phys. Commun. **178**, 524 (2008).
[54] F. Bruneval and X. Gonze, Phys. Rev. B **78**, 085125 (2008).
[55] J. A. Berger, L. Reining, and F. Sottile, Phys. Rev. B **85**, 085126 (2012).
[56] H. F. Wilson, F. Gygi, and G. Galli, Phys. Rev. B **78**, 113303 (2008).
[57] P. Umari, G. Stenuit, and S. Baroni, Phys. Rev. B **81**, 115104 (2010).
[58] F. Giustino, M. L. Cohen, and S. G. Louie, Phys. Rev. B **81**, 115105 (2010).
[59] S. Sharifzadeh, I. Tamblyn, P. Doak, P. T. Darancet, and J. B. Neaton, Eur. Phys. J. B **85**, 323 (2012).
[60] G. Samsonidze, M. Jain, J. Deslippe, M. L. Cohen, and S. G. Louie, Phys. Rev. Lett. **107**, 186404 (2011).
[61] L. Steinbeck, A. Rubio, L. Reining, M. Torrent, I. D. White, and R. W. Godby, Comput. Phys. Commun. **125**, 105 (2000).
[62] I. Vasiliev, S. Öğüt, and J. R. Chelikowsky, Phys. Rev. B **65**, 115416 (2002).
[63] I. Vasiliev, S. Öğüt, and J. R. Chelikowsky, Phys. Rev. B **60**, R8477 (1999).
[64] R. Schäfer and J. A. Becker, Phys. Rev. B **54**, 10296 (1996).
[65] D. O. Scanlon, C. W. Dunnill, J. Buckeridge, S. A. Shevlin, A. J. Logsdail, S. M. Woodley, C. R. A. Catlow, M. J. Powell, R. G. Palgrave, I. P. Parkin *et al.*, Nat. Mater. **12**, 798 (2013).

[66] G. Xiong, R. Shao, T. C. Droubay, A. G. Joly, K. M. Beck, S. A. Chambers, and W. P. Hess, Adv. Funct. Mater. **17**, 2133 (2007).
[67] J. C. Idrobo, M. Yang, K. A. Jackson, and S. Öğüt, Phys. Rev. B **74**, 153410 (2006).
[68] K. Baishya, J. C. Idrobo, S. Öğüt, M. Yang, K. Jackson, and J. Jellinek, Phys. Rev. B **78**, 075439 (2008).
[69] K. Baishya, J. C. Idrobo, S. Öğüt, M. Yang, K. A. Jackson, and J. Jellinek, Phys. Rev. B **83**, 245402 (2011).
[70] G. Mie, Ann. Phys. **330**, 377 (1908).
[71] R. Gans, Ann. Phys. **342**, 881 (1912).
[72] C. F. Bohren and D. R. Huffman, *Absorption and Scattering of Light by Small Particles* (Wiley-VCH, Weinheim, Germany, 1998).
[73] V. G. Grigoryan, M. Springborg, H. Minassian, and A. Melikyan, Comput. Theor. Chem. **1021**, 197 (2013).
[74] T. E. Tiwald and M. Schubert, Proc. SPIE **4103**, 19 (2000).
[75] M. L. Tiago and J. R. Chelikowsky, Phys. Status Solidi B **243**, 2151 (2006).